Chemical Physics 544 (2021) 111117

Contents lists available at ScienceDirect

Chemical Physics

journal homepage: www.elsevier.com/locate/chemphys

$BiSbWO_6$: Properties of a mixed 5s/6s lone-pair-electron system

Edan Bainglass [a,*], Aron Walsh [b,c], Muhammad N. Huda [a]

[a] Department of Physics, The University of Texas at Arlington, Arlington, TX 76019, USA
[b] Department of Materials, Imperial College London, London SW7 2AZ, United Kingdom
[c] Department of Materials Science & Engineering, Yonsei University, Seoul 07322, South Korea

ARTICLE INFO

Keywords:
Lone-pair-electrons
$BiSbWO_6$
Density functional theory
Post-transition metaloxides
Band-edge tuning

ABSTRACT

We investigate the behavior of lone-pair electrons in a mixed Sb(5s)/Bi(6s) crystal-environment. Density functional theory is used to calculate the electronic properties of Sb-alloyed-Bi_2WO_6 and to study the effects of introducing Sb 5s orbitals to the band structure. The band edge positions, partial charge analyses, and band decomposed charge densities of $BiSbWO_6$ are used to explain the observed trends in relative stabilities and band edge shifts. To isolate the role of the mixed lone-pair, we considered WO_3 as a control model. We find that local distortions caused by Sb 5s lone-pair electrons lead to upshifts in both valence and conduction band edges.

1. Introduction

Post-transition multinary metal oxides of electronic configuration ns^2-md^0 have been highlighted as efficient photocatalysts [1–3] due to their favorable optoelectronic properties. They can exhibit high hole-mobility arising from ns^2 – O 2p hybridization at their valence band maxima (VBM), which reduces O 2p localization. At their conduction band minima (CBM), np^0 – md^0 hybridization increases empty d-band dispersion, which improves electron mobility. Furthermore, the ns^2p^0 configuration of the post-transition cations can lead to unique crystal distortions due to the formation of stereochemically active electron lone pairs [4]. In such cases, the phenomenon has been further correlated with hybridizations of cation s-, p-, and anion p-orbitals, which altogether shape the frontier orbitals and determine their energetic position [5,6].

We recently studied one such system, namely $SbTa_{1-x}Nb_xO_4$ [7], in several common post-transition metal oxide phases, and found that varying the ionic/covalent character of the structure as a function of crystal phase and *n*d orbital contributions directly affected its overall stability and electronic properties. The layered structure of the orthorhombic stibiotantalite phase was found to be most stable. Moreover, its MO_6 layers (M = Ta, Nb) played a key role in determining the position of the band edges. These properties were influenced by the behavior of Sb 5s lone-pair electrons. In the present study, we clarify the effects of lone-pair electrons on the electronic structure of ns^2-md^0 materials. We show that variations in the lone-pair environment via isovalent alloying of the post-transition metal can shift band edge positions towards optimal values for photocatalytic water-splitting.

Of the ns^2-md^0 class of materials, none have received greater attention than $BiVO_4$. Regarded as a paradigm in photocatalytic semiconductor material research for its favorable properties, as well as its challenges [8–14], it has been extensively studied both experimentally and theoretically and is often used as a platform for designing new photocatalysts [15–18]. Due to the localized V 3d conduction orbitals, $BiVO_4$ charge transport properties are affected by the formation of small polaronic states [10,11,14]. Due to the poor transport properties, experimentally measured currents in $BiVO_4$ under visible light have come up short with respect to theoretically predicted values [13,14]. Alternatively, one may consider materials with more delocalized conduction bands, such as W $5d^0$ compounds. Here, the probability of forming polaronic trap states may be reduced allowing for higher charge carrier mobilities. One such example is the russellite mineral, or Bi_2WO_6, which itself has enjoyed a great deal of attention in photocatalysis research, though mostly under an experimental lens [19–24]. It has a suitable band gap range of 2.6–2.9 eV, with a VBM situated below the O_2 reduction potential allowing for oxygen evolution [25,26]. Its CBM, however, is slightly short of the H_2 reduction potential necessary for hydrogen evolution. Moreover, Bi_2WO_6 suffers from a high recombination rate, which limits its photocatalytic efficiency. This is often rationalized from the perspective of bulk defect states and/or surface morphologies that can lead to charge transfer paths longer than the carrier lifetime. Heterojunction design-schemes have been proposed to improve charge separation and mobility in Bi_2WO_6 [27–36]. Moreover, selective alloying has been shown to affect its band gap and band edge

* Corresponding author.
E-mail addresses: edan.bainglass@gmail.com (E. Bainglass), huda@uta.edu (M.N. Huda).

https://doi.org/10.1016/j.chemphys.2021.111117
Received 16 September 2020; Received in revised form 27 November 2020; Accepted 12 January 2021
Available online 23 January 2021

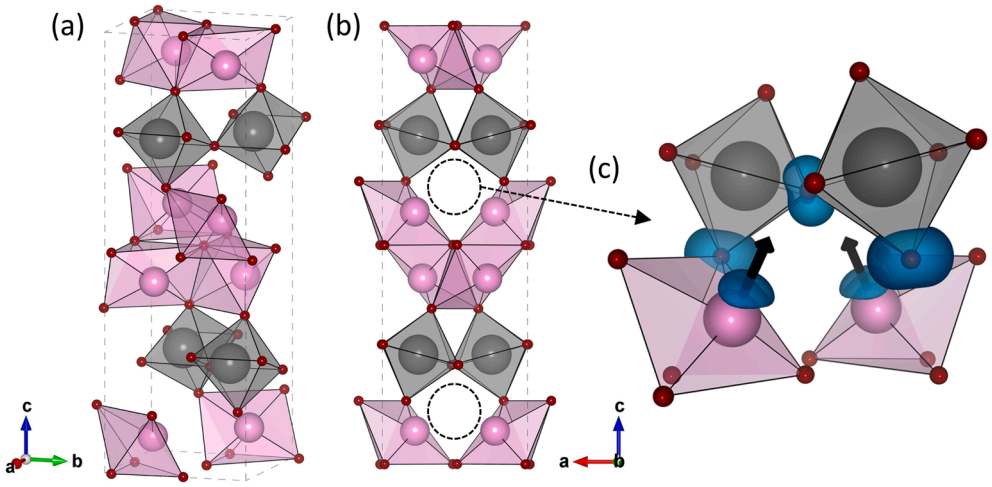

Fig. 1. (a) Bi_2WO_6 relaxed crystallographic unit cell. Pink polyhedra (top, bottom, and center) represent Bi_2O_2 layers; oxygen atoms are represented by dark red (smallest) spheres; WO_6 layers are shown in dark grey. (b) Bismuth lone-pair induced spatial voids are marked by dashed circles. (c) Lone-pair antibonding densities are drawn with an isosurface value of 0.015 $Å^{-3}$ (blue). Vectors mark lone-pair projections. (For interpretation of the references to colour in this figure legend, the reader is referred to the web version of this article.)

positions [26,37–39], improving its photocatalytic efficiency. We aim to combine and expand on these results.

The room-temperature γ-phase of Bi_2WO_6, known as the Aurivillius phase [40] – space group $P2_1ab$ (29) – is uniquely characterized by perovskite-like MO_6 layers (M = W, Mo) sandwiched between bismuth oxide layers. Various post-transition metals have been shown to retain the Aurivillius layered structure when introduced to the bismuth oxide matrix [41–45]. Interestingly, in the case of antimony, bismuth layers may be entirely replaced. This has led to the discovery of the Aurivillius-related phases Sb_2WO_6 [43] and Sb_2MoO_6 [46]. Castro et al. studied the structural evolution of $Bi_{2-x}Sb_xWO_6$ solid solutions and determined its stability up to $x = 1.5$, with larger values incurring a phase transition towards the ferroelastic triclinic phase of Sb_2WO_6 [44]. These solid solutions have also been studied for lithium ion battery applications [47] and photocatalysis [48]. To the best of our knowledge, the effects of isovalent Sb alloying on the electronic properties of Bi_2WO_6 have yet to be studied theoretically. Furthermore, the electronic structure of a mixed environment of varying stereochemical activities has not been explored. Lone-pair electrons of higher period post-transition cations tend to be less stereochemically active for a fixed anion species. Therefore, Sb 5s lone-pair electrons are expected to interact more strongly with the O environment compared to their Bi 6s counterpart, affecting both the crystal and electronic structures. In the present work, we investigate the electronic properties of $BiSbWO_6$, limiting the alloy composition to within the experimentally verified stable range [44], with emphasis on the effects of the mixed 5s/6s lone-pair environment on the band gap and band edge positions. The choice of Bi_2WO_6 as a design candidate addresses both abundancy and safety concerns, while the isovalent alloying scheme is expected to allow for simple processing. We briefly address the viability of $BiSbWO_6$ as a component in a proposed heterojunction architecture to facilitate charge transport and mobility.

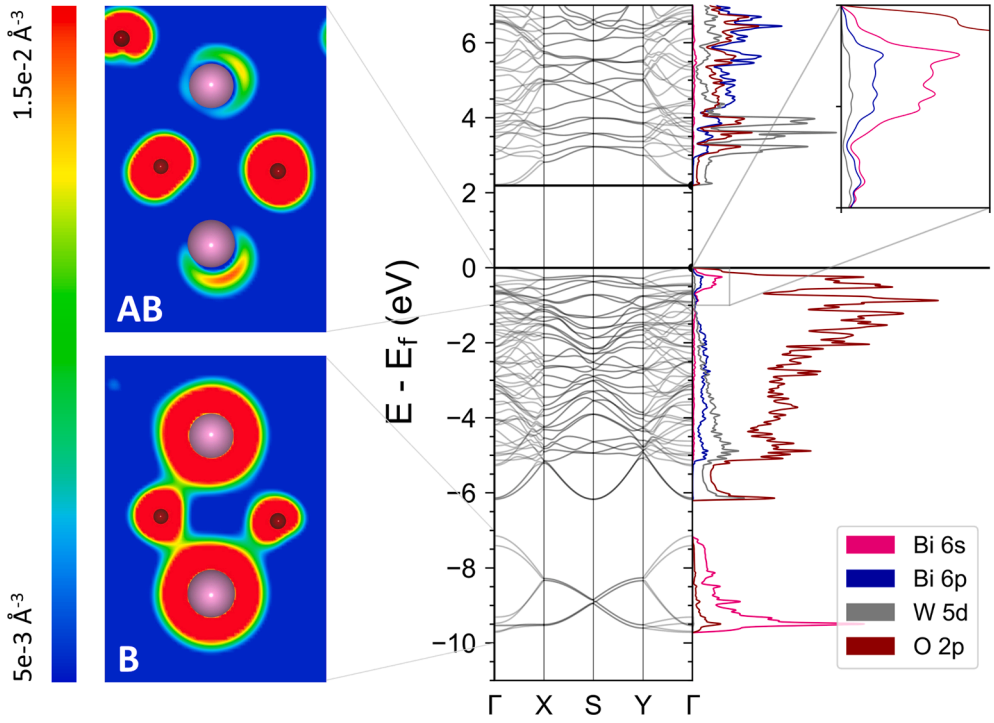

Fig. 2. Electronic band structure and density of states (right) for Bi_2WO_6. Band decomposed charge densities (left) are drawn for Bi 6s – O 2p bonding (B) and antibonding (AB) states. Antibonding contributions to the VBM are shown in the inset.

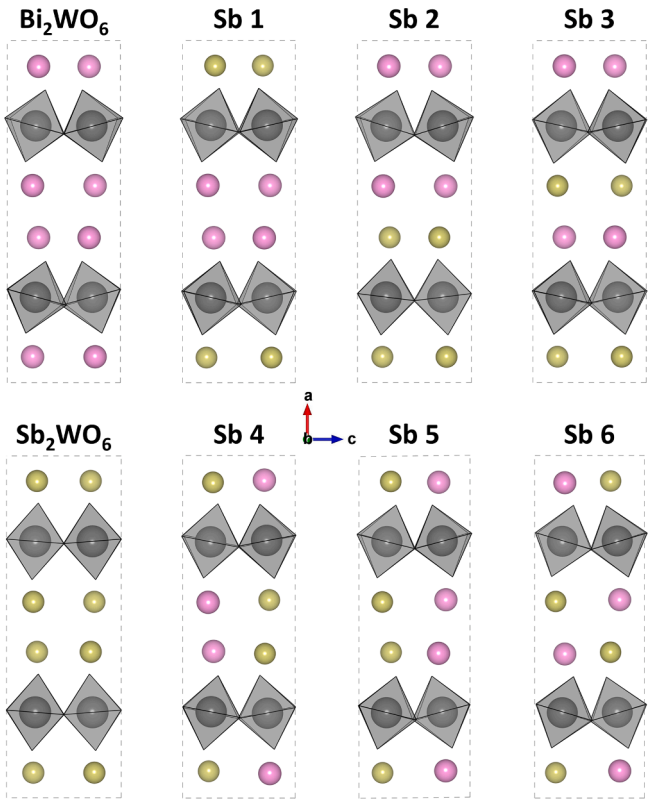

Fig. 3. Optimised units cells of $Bi_{2-x}Sb_xWO_6$. $BiSbWO_6$ (x = 1) configurations are labeled as Sb *i*. Oxygen sites are not shown for clarity. Sb is shown in green. WO_6 octahedra are shown to highlight variations in octahedral tilt in the presence of Sb 5s lone-pair electrons. (For interpretation of the references to colour in this figure legend, the reader is referred to the web version of this article.)

2. Methodology

We probe the crystal and electronic structures based on first-principles density functional theory (DFT) [49,50]. The Vienna ab initio Simulation Package (VASP 5.4.4) [51,52] plane-wave implementation of DFT is employed in calculating total energies, density of states, and electronic band structures for Bi_2WO_6 and its Sb–alloyed derivatives. The generalized gradient approximation formalism of Perdew, Burke, and Ernzerhof (GGA-PBE) [53,54] is used to approximate exchange and correlation contributions to the energy functional. The following valence electron configuration is considered: $Bi\{6s^25d^{10}6p^3\}$, $W\{5p^66s^25d^4\}$, $O\{2s^22p^4\}$, and $Sb\{5s^25p^3\}$. Remaining core electrons are modeled using the projector augmented wave methodology (PAW) [55,56]. Brillouin zone integrations are performed using a gaussian-like finite temperature approach [57] with σ (k_BT) = 0.01. The same is done for band structure calculations along high symmetry points. The tetrahedron method [58] is utilized for density of states (DOS) calculations. Monkhorst-Pack [59] *k*-space sampling of the Brillouin zone is implemented for all structures. Total energies are calculated with a $7 \times 7 \times 3$ *k*–mesh. DOS calculations are performed on a finer $11 \times 11 \times 5$ mesh. A plane wave cutoff of 600 eV is applied in all calculations. Both the *k*-mesh and plane wave cutoff values were systematically converged within a 1 meV difference in total energy. We apply a $[abc] \rightarrow [cab]$ transformation to the pristine Bi_2WO_6 unit cell (space group $Pc2_1b$) aligning the long lattice vector with the z-axis. Planes and directions are referenced with respect to this orientation. Unit cells are relaxed until ionic forces are less than 0.01 eV/Å. Symmetry constraints are applied in light of previous experimental findings [44]. Lastly, the known underestimation of band gaps by DFT-GGA [60–62] is ignored due to the comparative nature of the present study.

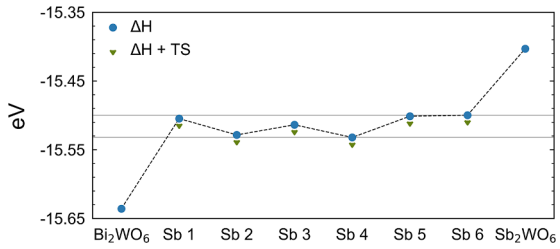

Fig. 4. Calculated formation enthalpies. Configurational entropy (TS) is added for $BiSbWO_6$ via Eq. (2). Formation enthalpies for $BiSbWO_6$ lie within a narrow ~ 30 meV band marked by solid lines.

3. Results and discussion

The relaxed crystal structure of Bi_2WO_6 is shown in Fig. 1(a). Calculated lattice parameters ($a = 5.563$ Å, $b = 5.605$ Å, $c = 16.857$ Å) are in good agreement with experimental diffraction measurements [63] considering the standard overestimation by GGA functionals [64]. The electronic structure of pristine Bi_2WO_6 is shown in Fig. 2. The width, dispersion, and spherical distribution of Bi 6s – O 2p bonding states between -10 and -7 eV, as well as the small O 2p contribution to the DOS at this range, all point to the weak stereochemical activity of Bi 6s lone-pair electrons. Bi 6s – O 2p antibonding densities form the upper valence band (inset) and project out into the spatial voids observed in Fig. 1(b) along the y-axis. Weak Bi 6s – O 2p interactions do not lead to high VBM band dispersion predicted in ns^2-md^0 materials, with a calculated hole effective mass of 3.5 m_0 (along the Γ-Y direction). In contrast, the CBM is less dependent on lone-pair electrons, as it is primarily comprised of W 5d – O 2p hybridized orbitals, with a calculated direct band gap of 2.19 eV about the Γ-point and an electron effective mass of 0.9 m_0 (along the Γ-Y direction). Based on this analysis, the introduction of Sb 5s electrons is likely to affect the upper valence band primarily while retaining the high dispersive nature of the lower conduction band. However, structural distortions due to substitutional alloying may affect the electronic structure. As seen in Fig. 1(c), Bi 6s – O 2p antibonding densities lead to tilting of adjacent WO_6 octahedra. MO_6 octahedral tilting has been shown to affect the band gap and band edge positions in ns^2-md^0 materials [7,65]. Radha et al. attributed a 0.1 eV difference in conduction band energy between Bi_2WO_6 and pyrochlore $BiFeWO_6$ to the influence of Fe 3d electrons on nearby WO_6 octahedra [26]. Hence, the CBM may indirectly depend on the mixed lone-pair environment via local structural distortions.

To explore the configurational space of $BiSbWO_6$, we selected six representative input geometries, each designated as Sb *i*. In configurations Sb 1–3, dopants are placed into (001) layers to probe the layered nature of the Aurivillius phase. In Sb 4–6, Sb is intermixed within Bi_2O_2 layers. The relaxed $BiSbWO_6$ structure models are shown in Fig. 3. Their relative stability is measured through calculated formation enthalpies, ΔH_f, obtained from [66]

$$\Delta H_f = E(m) - \sum_x n_x E(x)_{bulk} \quad (1)$$

where $E(m)$ is the calculated total energy of configuration m, and $E(x)_{bulk}$ is the total energy of the common bulk phase of constituent x multiplied by the its number of sites n_x. Note that for oxygen, we consider the total energy of an oxygen dimer in the calculation. A more negative formation enthalpy indicates greater relative stability. Fig. 4 shows that calculated formation enthalpies for the six configurations lie within a narrow ~ 30 meV window, on the order of k_BT at room temperature. Additional calculations were performed on four $2 \times 2 \times 1$ Bi_2WO_6 supercells, each with a random sample of half its Bi sites substituted for Sb. The calculated formation enthalpies of the four supercells lie within an even-narrower range of ~ 10 meV roughly in the middle of the ~ 30 meV window. Hence, we argue that during synthesis,

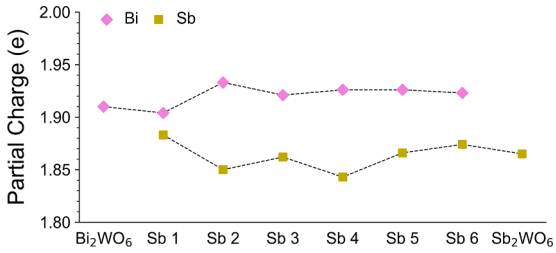

Fig. 5. Partial charge of post-transition sites calculated by subtracting average Bader charges from the number of valence electrons per element. Sb partial charge follows the same trend as formation entahlpies in the six selected $BiSbWO_6$ configurations (Fig. 4). W and O exhibit constant partial charges of 2.87 and -1.11, respectively.

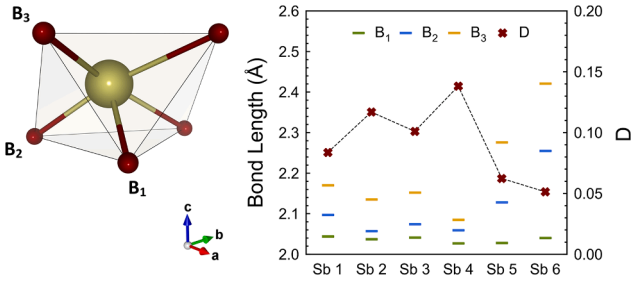

Fig. 6. Baur distortion indices (D) and selected bond lengths for a representative Sb polyhedron across the six $BiSbWO_6$ configurations. Higher distortion reflects a larger Sb cationic shift towards one end of the polyhedron.

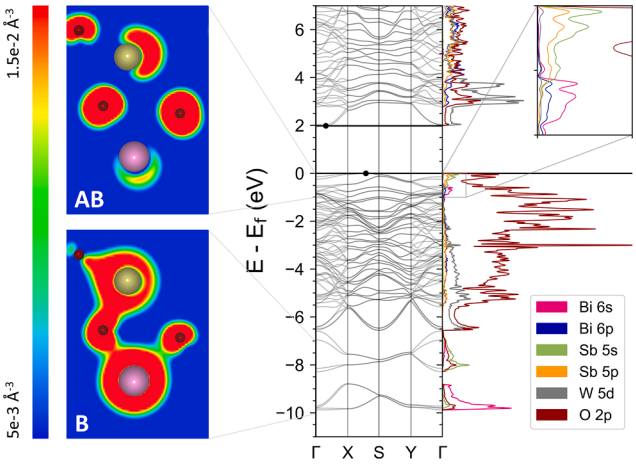

Fig. 7. Band structure and density of states (right) for the Sb 4 configuration of $BiSbWO_6$. Band decomposed charge densities (left) show the contrast between the spherically symmetric Bi 6s – O 2p and asymmetric Sb 5s – O 2p bonding (B) states. A significantly larger antibonding (AB) density is projected away from Sb sites and contributes more states near the valence band maximum (inset).

$BiSbWO_6$ may form as an ensemble of many possible configurations resulting in a homogeneous distribution of Sb and W ions. This suggestion merits an examination of configurational entropy in the system. An approximation of configurational entropic contributions to the overall stability of a compound in the presence of substitutional impurities can be obtained from [67]

$$S = -k_B \sum_{i=1}^{N} x_i \log(x_i) \tag{2}$$

where N is the number of sites available for substitution – taking limiting factors into account such as the oxidation states of the relevant species and charge neutrality – x_i is the relative composition of species i, and k_B is Boltzmann's constant. The maximum entropy occurs at equal compositions. For $x_{Bi} = x_{Sb}$, configurational entropy lowers energies by $\sim$ 8 meV at 300 K, which is not significant enough to shift the relative stability band of $Bi_{2-x}Sb_xWO_6$ beyond its extreme configurations (x = 0, 2).

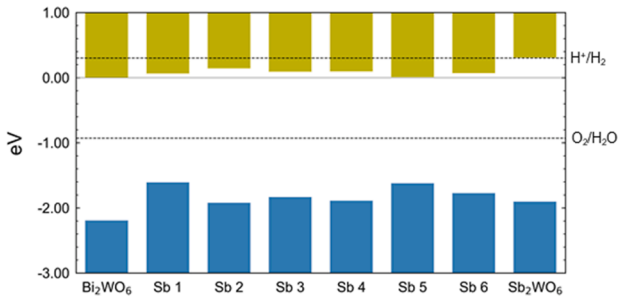

Fig. 8. Aligned valence (blue) and conduction (green) band energies for the Sb/Bi end member compounds and six alloy models (alloy symbols Sb i are defined in Fig. 3). A globally averaged O 1s core state is used as a reference. The Bi_2WO_6 conduction band is set to 0 eV. The water redox potentials are shown in dashed lines and are positioned with respect to the empirically derived conduction band edge of Bi_2WO_6 (see text for reference). (For interpretation of the references to colour in this figure legend, the reader is referred to the web version of this article.)

Although Bi and Sb both have the same formal oxidation state of 3^+ in this system, Bader partial charge analysis [68–72] gives a lower effective charge for Sb compared to Bi (Fig. 5), which agrees with their relative electronegativities. Despite the small differences in formation enthalpies, comparing Figs. 4 and 5 suggests they may be correlated with the partial charge of Sb, as both follow a similar trend across the six selected configurations of $BiSbWO_6$. We attribute this to the degree to which Sb 5s – O 2p orbitals overlap. The closer proximity of Sb 5s and O 2p energy levels [5] provides a path for stabilizing the given configuration through orbital hybridization. Increased proximity of Sb and O sites leads to greater orbital overlap and consequently a more stable system. In Fig. 6, we measure Sb cationic shifts in $BiSbWO_6$ via Baur distortion indices [73] and Sb-O bond lengths. Distortion indices mirror formation enthalpies across all configurations. We note that Sb 4 – the most stable configuration – exhibits the highest distortion, indicating the largest Sb cationic shift resulting in the shortest Sb-O bonds. Similar reasoning explains the poor stability of the Sb 6 configuration. The electronic structure of Sb 4 is given in Fig. 7. Bi 6s – O 2p bonding states retain their spherical distribution in the mixed lone-pair environment. Sb 5s – O 2p bonding states, on the other hand, are asymmetric, with delocalized charge shifting towards the nearest O sites. The magnitude of the Sb 5s – O 2p antibonding charge density is significantly larger and takes over the VBM with near double the density of states (inset). This results in a narrower, though now indirect band gap (1.98 eV). The stronger Sb 5s – O 2p interaction also reduces the hole effective mass to 3.1 m_0 (X-S). W 5d – O 2p states retain their high dispersion, with an electron effective mass of 0.8 m_0 (Γ-X). Overall, Sb-in-Bi substitution improves carrier mobility.

To compare $BiSbWO_6$ band edge positions on an equal footing, we align the bands by referencing VBM/CBM levels to the deep O 1s core level. This reference state was averaged over all O sites and across all $Bi_{2-x}Sb_xWO_6$ configurations. The results are shown in Fig. 8. The water redox potentials are shown with respect to an empirically derived CBM level for Bi_2WO_6 [26]. In all cases, Sb 5s – O 2p antibonding states upshift the valence band with respect to the pristine cell. We note that the largest upshift (0.57 eV) leaves the VBM well below the water oxidation potential. More interestingly, conduction band upshifts are also observed across the board and follow a similar trend of the distortion indices. This suggests that local structural distortions about Sb sites do exert an influence on the nearby WO_6 layers and indirectly affect the

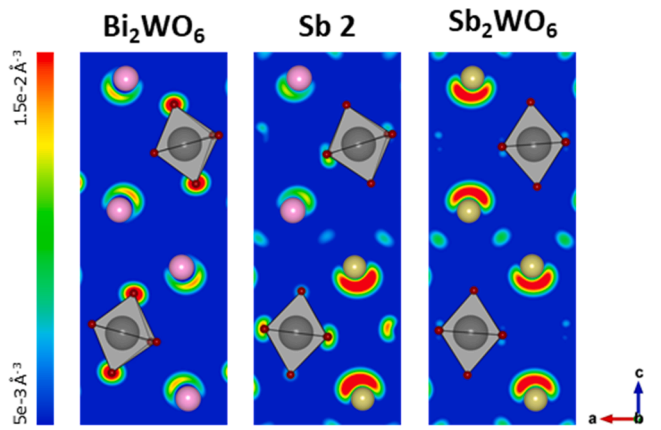

Fig. 9. Band decomposed charge densities showing the dependency of WO_6 octahedral tilt on the magnitude of neighboring *ns* – O 2p antibonding densities. Sb 2 refers to the mixed Sb/Bi model shown in Fig. 3.

conduction band energy. The largest upshift among the $BiSbWO_6$ configurations is seen in Sb 2 (0.14 eV). We note that in the Sb 2 configuration, one WO_6 layer is sandwiched between Sb_2O_2 layers (Fig. 3), which appears to decrease octahedral tilting in the WO_6 layer. This configuration is effectively doubled in the Sb-rich Sb_2WO_6 case, where the CBM upshift is 0.31 eV. We showed in Fig. 1(c) that WO_6 octahedral tilting occurs in the presence of lone-pair antibonding densities. We investigate this further by comparing the charge densities of Bi_2WO_6, Sb 2, and Sb_2WO_6 antibonding states (Fig. 9). Sb 5s – O 2p antibonding densities align more strongly along the z-axis and interact with O sites at the nearest corners of WO_6 octahedra, which consequently reduces their tilt. This Sb-O-W interaction can be seen in the DOS of Sb 4 (Fig. 7), where Sb 5s – O 2p and W 5d – O 2p bonding states overlap at the bottom edge of the valence band. We later show that this overlap is directly proportional to the CBM upshift.

To better understand how WO_6 octahedral tilting affects the band structure, we manually tilt a single layer of WO_6 octahedra in monoclinic WO_3. The binary oxide is chosen for its similar W-O environment and the absence of s^2 lone-pair cations. In Fig. 10, we compare the band structure of three WO_3 unit cells. The fully relaxed unit cell represents the control case. In the other two cells, we manually twist WO_6 octahedra in a single layer, keeping the adjacent layer in its relaxed geometry. In the band structure, we mark three bands of interest. The W 5d – O 2p antibonding state is shown in green. The bonding state of the frozen (distorted) layer is in blue (orange). Reducing the applied distortion back towards the relaxed geometry – from Fig. 10(a) to (c) – causes a

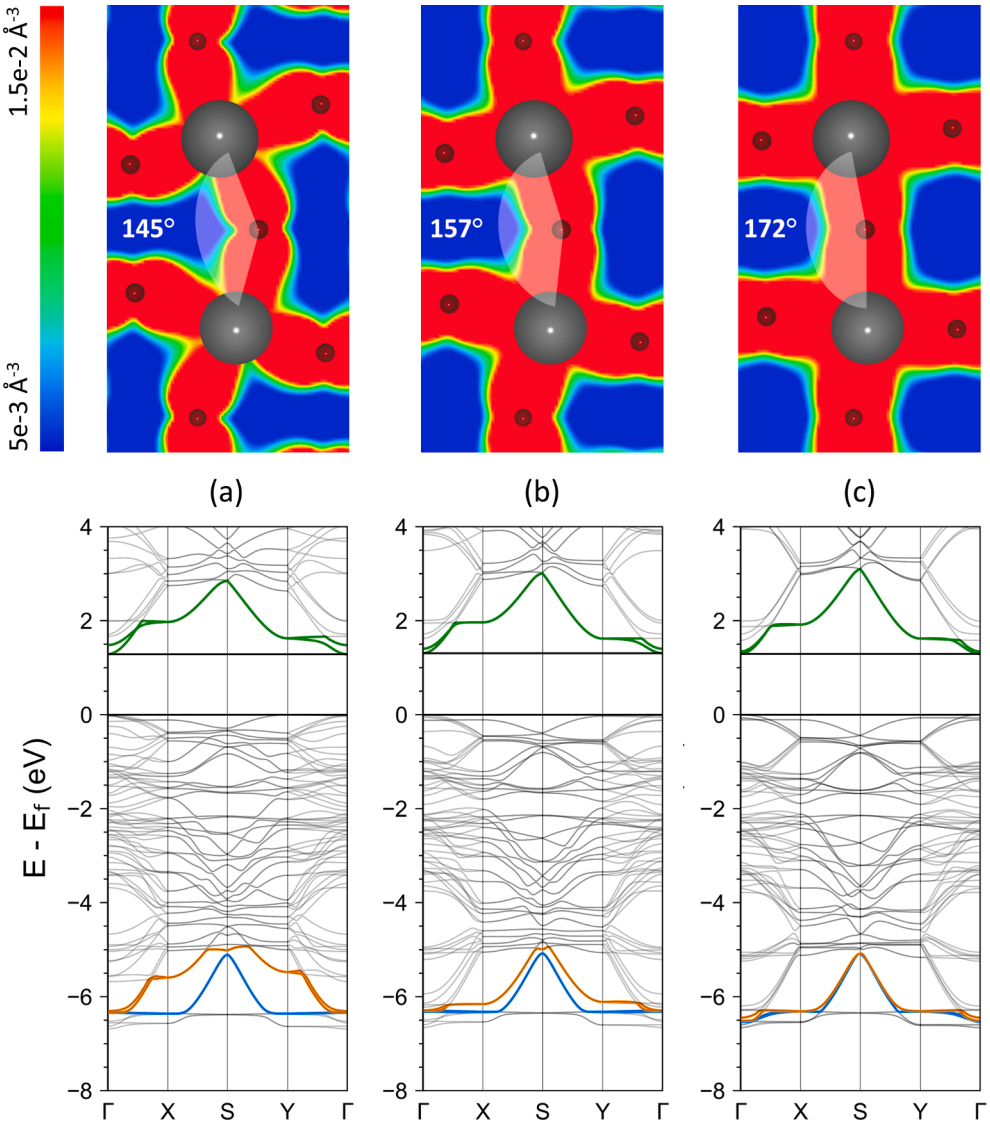

Fig. 10. Band structures and band decomposed charge densities for monoclinic WO_3 with manually applied tilting resulting in (a) 145° and (b) 157° W-O-W angles. The relaxed unit cell (c) exhibits a W-O-W angle of 172° and is used for control. Charge densities are projected onto the bonding states at the bottom of the valence band. The W 5d – O 2p bonding state for the distorted (fixed) layer is shown in orange (blue). The corresponding antibonding state is in green. (For interpretation of the references to colour in this figure legend, the reader is referred to the web version of this article.)

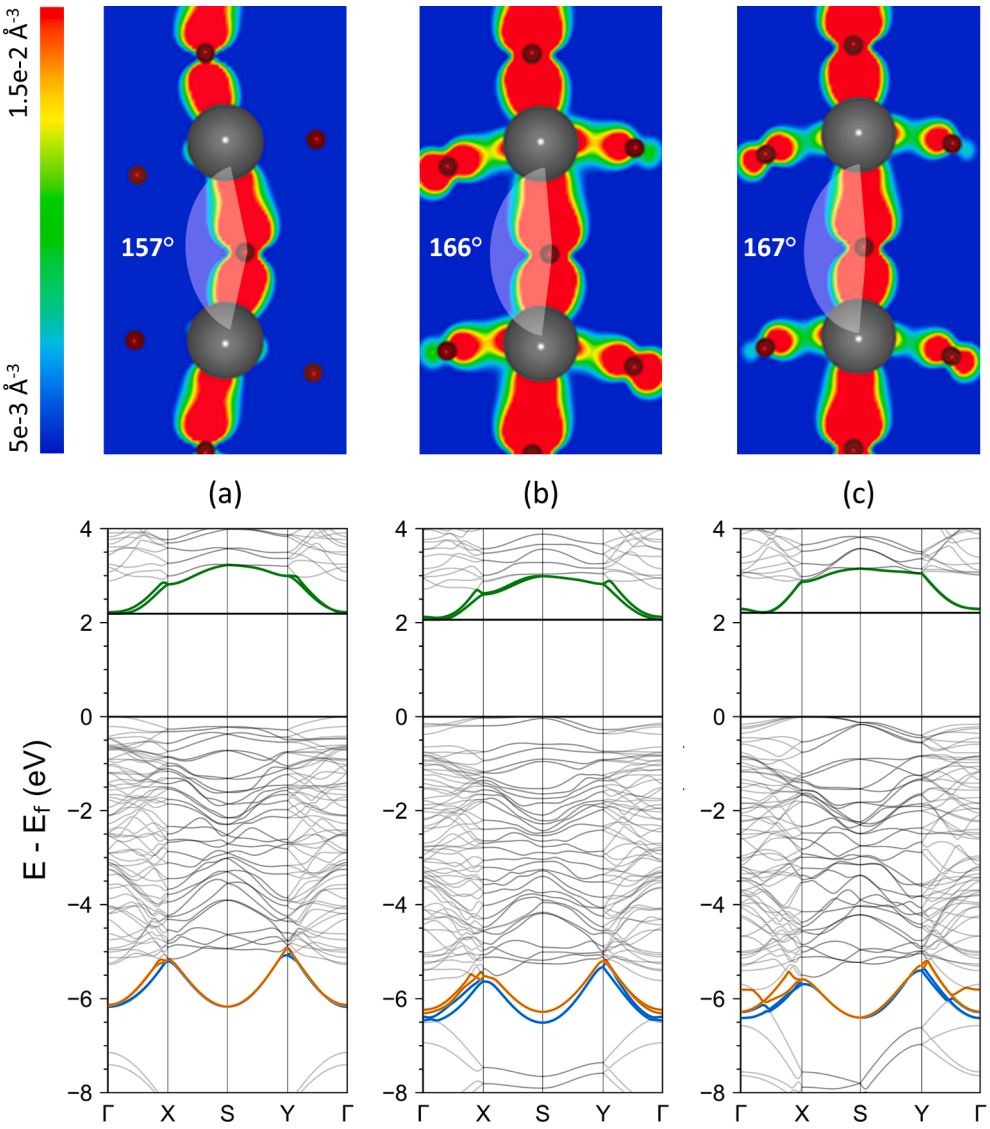

Fig. 11. Band structures and band decomposed charge densities for (a) Bi_2WO_6, (b) Sb 2, and (c) Sb_2WO_6. Charge densities are projected onto the bonding state of the lower WO_6 layer. The W 5d – O 2p bonding state for the top (bottom) WO_6 layer is shown in orange (blue). The corresponding antibonding state is in green. (For interpretation of the references to colour in this figure legend, the reader is referred to the web version of this article.)

downshift of the distorted bonding state. Its antibonding counterpart at the CBM near the Γ-point gradually upshifts and becomes degenerate with that of the frozen layer. We attribute this to bonding-antibonding splitting due to increasing W 5d – O 2p hybridization. This is apparent in band decomposed charge densities, as well as in average W-O bond lengths, with 2.006 Å at the highest distortion and 1.945 Å in the relaxed cell. Hence, reduced tilting of WO_6 octahedra with respect to one another results in shorter W-O bond lengths and increased W 5d – O 2p hybridization. This in turn raises the conduction band.

We now apply the same reasoning to the relaxed models of Bi_2WO_6, Sb 2, and Sb_2WO_6. In Fig. 11, we project the charge density of each unit cell onto the bonding state of its lower WO_6 layer. We first note that in $Bi_{2-x}Sb_xWO_6$, the natural driving force behind the twisting of WO_6 octahedra is the apparent onset of hybridization about the W-O-Sb bonding network clearly missing in the Bi_2WO_6 charge density. This does appear to increase hybridization within the WO_6 layer. However, unlike in monoclinic WO_3, the average W-O bond lengths do not decrease monotonically – 1.977 Å in Bi_2WO_6 (Fig. 11a), 1.971 Å in Sb 2 (Fig. 11b), and 1.984 Å in Sb_2WO_6 (Fig. 11c). Similarly, the hybridization about the W-O-W bonding network increases in Sb 2 but decreases slightly in Sb_2WO_6. To explain the position of their conduction band edges, we point to the asymmetric alloying scheme of Sb 2. The WO_6 layer surrounded by Sb has a W-O-W bond angle of 166°, greater than the 153° angle measured in Bi_2WO_6. However, the WO_6 layer surrounded by Bi exhibits a 151° angle, as well as longer average W-O bond lengths (1.990 Å). Therefore, the stronger hybridization in the lower WO_6 layer of Sb 2 does lead to a bonding-antibonding splitting of W 5d – O 2p states observed in Fig. 11(b), but the lack of Sb 5s interactions in its upper WO_6 layer leaves the corresponding bonding and antibonding states lagging behind. This reduces the overall magnitude of the CBM upshift. Though Sb_2WO_6 exhibits reduced hybridization in the lower WO_6 layer – resulting in a lesser bonding-antibonding splitting – the identical splitting occurring in its upper WO_6 layer results in both conduction bands shifting upwards. The larger 167° W-O-W in the lower WO_6 layer of Sb_2WO_6 compared to the 151° in the upper WO_6 layer of Sb 2 suggests that the degenerate CBM of the former is situated above the conduction band of the latter. This explains its higher CBM.

The configuration of Sb 2, in which WO_6 layers are sandwiched between single-post-transition-metal species, offers an interesting opportunity for facile heterojunction design as a natural extension of the pristine cell. Such crystal engineering could be used to enhance both light absorption and charge carrier separation, reducing non-radiative

losses and improving photocatalytic efficiency. We find that the Sb 2 configuration is well-suited for forming a heterostructure, as its in-plane lattice parameters ($a = 5.558$ Å; $b = 5.682$ Å) are within 1% of Bi_2WO_6 ($a = 5.563$ Å; $b = 5.605$ Å). Although it is not the most stable configuration (within the 30 meV group), it may be accessible through epitaxial growth. This is a valuable direction for further study.

4. Conclusions

In studying the configurational space of $BiSbWO_6$, we provided new insight into the behavior of lone-pair electrons in mixed post-transition metal oxides. We showed that the band gap and band edge positions of Bi_2WO_6 can be controlled by manipulating the chemical interactions of WO_6 layers via Sb-in-Bi substitutions. We found that the higher stereochemical activity of Sb 5s lone-pair electrons led to stronger Sb 5s – O 2p hybridization, which upshifted the VBM by up to 0.57 eV. We also showed that local structure distortions due to Sb 5s lone-pair antibonding densities reduced WO_6 octahedral tilting. Increased W 5d – O 2p hybridization in response to the alignment of WO_6 octahedra resulted in greater bonding-antibonding splitting. This was shown to upshift the conduction band edge of $BiSbWO_6$ by up to 0.14 eV. In the case of Sb_2WO_6, reduced octahedral tilting led to a CBM upshift of 0.31 eV. Overall, $BiSbWO_6$ band shifts resulted in narrower band gaps with respect to Bi_2WO_6.

The narrow stability range observed for the six studied $BiSbWO_6$ configurations, with a contribution of 8 meV due to configurational entropy stabilization, suggests a possible mixture of phases during synthesis, which may result in an ensemble averaging of the electronic properties. We suggest one candidate for heterojunction formation due to its low lattice mismatch with Bi_2WO_6. These insights may be further extended and applied to mixed post-transition metal oxides more generally in pursuit of new efficient solar absorbing materials.

CRediT authorship contribution statement

Edan Bainglass: Conceptualization, Formal analysis, Investigation, Software, Validation, Visualization, Writing - original draft. **Aron Walsh:** Validation, Funding acquisition. **Muhammad N. Huda:** Conceptualization, Formal analysis, Funding acquisition, Project administration, Supervision, Writing - original draft.

Declaration of Competing Interest

The authors declare that they have no known competing financial interests or personal relationships that could have appeared to influence the work reported in this paper.

Acknowledgements

This work was supported by the National Science Foundation (NSF) grant #1609811. All calculations were performed on Texas Advanced Computing Center (TACC) servers. Additional support was received from a National Research Foundation of Korea (NRF) grant funded by the Korean government (MSIT) (No. 2018R1C1B6008728).

References

[1] N. Saito, H. Kadowaki, H. Kobayashi, K. Ikarashi, H. Nishiyama, Y. Inoue, A new photocatalyst of RuO2-loaded PbWO4 for overall splitting of water, Chem. Lett. 33 (11) (2004) 1452–1453.
[2] H. Kadowaki, N. Saito, H. Nishiyama, H. Kobayashi, Y. Shimodaira, Y. Inoue, Overall splitting of water by RuO2-loaded PbWO4 photocatalyst with d10s2-d0 configuration, J. Phys. Chem. C. 111 (1) (2007) 439–444.
[3] C. Janáky, K. Rajeshwar, N.R. de Tacconi, W. Chanmanee, M.N. Huda, Tungsten-based oxide semiconductors for solar hydrogen generation, Catal. Today. 199 (2013) 53–64.
[4] I. Hargittai, B. Chamberland, The VSEPR model of molecular geometry, Comput. Math. Appl. 12 (3-4) (1986) 1021–1038.
[5] A. Walsh, D.J. Payne, R.G. Egdell, G.W. Watson, Stereochemistry of post-transition metal oxides: revision of the classical lone pair model, Chem. Soc. Rev. 40 (2011) 4455.
[6] C.E. Mohn, S. Stølen, Influence of the stereochemically active bismuth lone pair structure on ferroelectricity and photocalytic activity of Aurivillius phase Bi 2WO6, Phys. Rev. B – Condens. Matter Mater. Phys. 83 (2011) 14103.
[7] E. Bainglass, M.N. Huda, Electronic properties of SbTa1-xNbxO4: Phase-related distortions, J. Electrochem. Soc. 166 (5) (2019) H3195–H3201.
[8] A. Walsh, Y. Yan, M.N. Huda, M.M. Al-Jassim, S.H. Wei, Band edge electronic structure of BiVO 4: Elucidating the role of the Bi s and V d orbitals, Chem. Mater. 21 (2009) 547–551.
[9] W. Li, X. Wang, Z.e. Wang, Y.i. Meng, X. Sun, T. Yan, J. You, D. Kong, Relationship between crystalline phases and photocatalytic activities of BiVO4, Mater. Res. Bull. 83 (2016) 259–267.
[10] K.E. Kweon, G.S. Hwang, J. Kim, S. Kim, S.M. Kim, Electron small polarons and their transport in bismuth vanadate: A first principles study, Phys. Chem. Chem. Phys. 17 (1) (2015) 256–260.
[11] A.J.E. Rettie, W.D. Chemelewski, D. Emin, C.B. Mullins, Unravelling small-polaron transport in metal oxide photoelectrodes, J. Phys. Chem. Lett. 7 (3) (2016) 471–479.
[12] T. Saison, N. Chemin, C. Chanéac, O. Durupthy, L. Mariey, F. Maugé, V. Brezová, J.-P. Jolivet, New Insights Into BiVO 4 properties as visible light photocatalyst, J. Phys. Chem. C. 119 (23) (2015) 12967–12977.
[13] Y. Hermans, A. Klein, K. Ellmer, R. van de Krol, T. Toupance, W. Jaegermann, Energy-band alignment of BiVO 4 from photoelectron spectroscopy of solid-state interfaces, J. Phys. Chem. C. 122 (36) (2018) 20861–20870.
[14] Y. Hermans, S. Murcia-López, A. Klein, R. van de Krol, T. Andreu, J.R. Morante, T. Toupance, W. Jaegermann, Analysis of the interfacial characteristics of BiVO 4 /metal oxide heterostructures and its implication on their junction properties, Phys. Chem. Chem. Phys. 21 (9) (2019) 5086–5096.
[15] O. Monfort, G. Plesch, Bismuth vanadate-based semiconductor photocatalysts: A short critical review on the efficiency and the mechanism of photodegradation of organic pollutants, Environ. Sci. Pollut. Res. 25 (2018) 19362–19379.
[16] A. Malathi, J. Madhavan, M. Ashokkumar, P. Arunachalam, A review on BiVO 4 photocatalyst: Activity enhancement methods for solar photocatalytic applications, Appl. Catal. A Gen. 555 (2018) 47–74.
[17] I.D. Sharp, J.K. Cooper, F.M. Toma, R. Buonsanti, Bismuth vanadate as a platform for accelerating discovery and development of complex transition-metal oxide photoanodes, ACS Energy Lett. 2 (1) (2017) 139–150.
[18] H.P. Sarker, P.M. Rao, M.N. Huda, Niobium doping in BiVO4: Interplay between effective mass Stability, and Pressure, Chem. Phys. Chem. 20 (2019) 773–784.
[19] T. Saison, P. Gras, N. Chemin, C. Chanéac, O. Durupthy, V. Brezová, C. Colbeau-Justin, J.-P. Jolivet, New insights into Bi2WO6 properties as a visible-light photocatalyst, J. Phys. Chem. C. 117 (44) (2013) 22656–22666.
[20] X. Ding, K. Zhao, L. Zhang, Enhanced photocatalytic removal of sodium pentachlorophenate with self-doped Bi 2 WO 6 under visible light by generating more superoxide ions, Environ. Sci. Technol. 48 (10) (2014) 5823–5831.
[21] C. Zhang, Y. Zhu, Synthesis of square Bi2WO6 nanoplates as high-activity visible-light-driven photocatalysts, Chem. Mater. 17 (13) (2005) 3537–3545.
[22] N. Zhang, R. Ciriminna, M. Pagliaro, Y.-J. Xu, Nanochemistry-derived Bi 2 WO 6 nanostructures: towards production of sustainable chemicals and fuels induced by visible light, Chem. Soc. Rev. 43 (2014) 5276–5287.
[23] S. Girish Kumar, K.S.R. Koteswara Rao, Tungsten-based nanomaterials (WO 3 & Bi 2 WO 6): Modifications related to charge carrier transfer mechanisms and photocatalytic applications, Appl. Surf. Sci. 355 (2015) 939–958.
[24] J. Tang, Z. Zou, J. Ye, Photocatalytic decomposition of organic contaminants by Bi 2WO6 under visible light irradiation, Catal. Lett. 92 (1/2) (2004) 53–56.
[25] F. Ren, J. Zhang, Y. Wang, Enhanced photocatalytic activities of Bi2WO6 by introducing Zn to replace Bi lattice sites: A first-principles study, RSC Adv. 5 (2015) 29058–29065.
[26] R. Radha, A. Srinivasan, P. Manimuthu, S. Balakumar, Tailored sunlight driven nano-photocatalyst: bismuth iron tungstate (BiFeWO6), J. Mater. Chem. C. 3 (39) (2015) 10285–10292.
[27] M. Ge, Y. Li, L. Liu, Z. Zhou, W. Chen, Bi2O3?Bi2WO6 composite microspheres: Hydrothermal synthesis and photocatalytic performances, J. Phys. Chem. C. 115 (2011) 5220–5225.
[28] X. Zhang, Y. Gong, X. Dong, X. Zhang, C. Ma, F. Shi, Fabrication and efficient visible light-induced photocatalytic activity of Bi 2WO 6/BiVO 4 heterojunction, Mater. Chem. Phys. 136 (2-3) (2012) 472–476.
[29] Z. Zhu, Y. Yan, J. Li, Synthesis of flower-like WO3/Bi2WO6 heterojunction and enhanced photocatalytic degradation for Rhodamine B, Micro Nano Lett. 10 (9) (2015) 460–464.
[30] Z. Liu, Q. Yu, J. Liu, T. Li, F. Huang, Enhanced visible photocatalytic activity in flower-like CuO-WO3-Bi2WO6 ternary hybrid through the cascadal electron transfer, Micro Nano Lett. 12 (3) (2017) 195–200.
[31] S. Li, S. Hu, W. Jiang, Y. Liu, J. Liu, Z. Wang, Facile synthesis of flower-like Ag3VO4/Bi2WO6 heterojunction with enhanced visible-light photocatalytic activity, J. Colloid Interface Sci. 501 (2017) 156–163.
[32] L. Jiang, S. Wang, L. Shi, Y. Zhao, Z. Wang, M. Zhang, S. Yuan, Solvothermal synthesis of TiO 2 /Bi 2 WO 6 heterojunction photocatalyst with optimized interface structure and enabled photocatalytic performance, Chinese J. Chem. 35 (2) (2017) 183–188.
[33] F. Opoku, K.K. Govender, C.G.C.E. van Sittert, P.P. Govender, Insights into the photocatalytic mechanism of mediator-free direct Z-scheme g-C 3 N 4 /Bi 2 MoO 6 (010) and g-C 3 N 4 /Bi 2 WO 6 (010) heterostructures: A hybrid density functional theory study, Appl. Surf. Sci. 427 (2018) 487–498.

[34] J. Jia, P. Xue, R. Wang, X. Bai, X. Hu, J. Fan, E. Liu, The Bi/Bi 2 WO 6 heterojunction with stable interface contact and enhanced visible-light photocatalytic activity for phenol and Cr(VI) removal, J. Chem. Technol. Biotechnol. 93 (10) (2018) 2988–2999.
[35] Q. Guo, Y. Huang, H. Xu, D. Luo, F. Huang, L. Gu, Y. Wei, H. Zhao, L. Fan, J. Wu, The effects of solvent on photocatalytic properties of Bi 2 WO 6 /TiO 2 heterojunction under visible light irradiation, Solid State Sci. 78 (2018) 95–106.
[36] X. Lu, W. Che, X. Hu, Y. Wang, A. Zhang, F. Deng, S. Luo, D.D. Dionysiou, The facile fabrication of novel visible-light-driven Z-scheme CuInS2/Bi2WO6 heterojunction with intimate interface contact by in situ hydrothermal growth strategy for extraordinary photocatalytic performance, Chem. Eng. J. 356 (2019) 819–829.
[37] L. Zhang, Y. Man, Y. Zhu, Effects of Mo replacement on the structure and visible-light-induced photocatalytic performances of Bi2WO6 photocatalyst, ACS Catal. 1 (8) (2011) 841–848.
[38] C. Bhattacharya, H.C. Lee, A.J. Bard, Rapid screening by scanning electrochemical microscopy (SECM) of dopants for Bi2WO6 improved photocatalytic water oxidation with Zn doping, J. Phys. Chem. C. 117 (19) (2013) 9633–9640.
[39] A. Phuruangrat, P. Dumrongrojthanath, S. Thongtem, T. Thongtem, Hydrothermal synthesis of I-doped Bi2WO6 for using as a visible-light-driven photocatalyst, Mater. Lett. 224 (2018) 67–70.
[40] B. Aurivillius, Structures of Bi2NbO5F and isomorphous compounds, Ark. Foer Kemi. 5 (1952) 39–47.
[41] P. Millán, A. Castro, J.B. Torrance, The first doping of lead2+ into the bismuth oxide layers of the aurivillius oxides, Mater. Res. Bull. 28 (2) (1993) 117–122.
[42] A. Castro, P. Millan, M. Martinezlope, J. Torrance, Substitutions for Bi3+ into (Bi2O2)2+ layers of the Aurivillius (Bi2O2)(An-1BnO3n+1) oxides, Solid State Ionics. 63-65 (1993) 897–901.
[43] A. Castro, P. Millan, R. Enjalbert, E. Snoeck, J. Galy, An original oxide of antimony and tungsten related to aurivillius phases, Mater. Res. Bull. 29 (8) (1994) 871–879.
[44] A. Castro, P. Millan, R. Enjalbert, Structural evolution of the Aurivillius framework in the solid solutions Bi2WO6-Sb2WO6, Mater. Res. Bull. 30 (7) (1995) 871–882.
[45] P. Millan, A. Ramirez, A. Castro, Substitutions of smaller Sb 3+ and Sn 2+ cations for Bi 3+ in Aurivillius-like phases, Mater. Sci. Lett. 14 (23) (1995) 1657–1660.
[46] C.D. Ling, R.L. Withers, A.D. Rae, S. Schmid, J.G. Thompson, Antiferroelectric modulations in Sb2WO6 and Sb2MoO6, Acta Crystallogr. Sect. B Struct. Sci. 52 (4) (1996) 610–615.
[47] A. Martínez-de la Cruz, F.E. Longoria Rodríguez, Electrochemical lithium insertion in the solid solution Bi2WO6-Sb2WO6 with Aurivillius framework, Mater. Res. Bull. 42 (10) (2007) 1851–1855.
[48] A. Singh, D.P. Dutta, M. Roy, A.K. Tyagi, M.H. Fulekar, Sonochemical synthesis, characterization, and photocatalytic properties of Bi 2–x Sb x WO 6 nanorods, J. Mater. Sci. 49 (5) (2014) 2085–2097.
[49] P. Hohenberg, W. Kohn, Inhomogeneous electron gas, Phys. Rev. 136 (3B) (1964) B864–B871.
[50] W. Kohn, L.J. Sham, Self-consistent equations including exchange and correlation effects, Phys. Rev. 140 (4A) (1965) A1133–A1138.
[51] G. Kresse, J. Furthmüller, Efficiency of ab-initio total energy calculations for metals and semiconductors using a plane-wave basis set, Comput. Mater. Sci. 6 (1) (1996) 15–50.
[52] G. Kresse, J. Furthmüller, Efficient iterative schemes for ab initio total-energy calculations using a plane-wave basis set, Phys. Rev. B - Condens. Matter Mater. Phys. 54 (16) (1996) 11169–11186.
[53] J.P. Perdew, J.A. Chevary, S.H. Vosko, K.A. Jackson, M.R. Pederson, D.J. Singh, C. Fiolhais, Atoms, molecules, solids, and surfaces: Applications of the generalized gradient approximation for exchange and correlation, Phys. Rev. B. 46 (1992) 6671–6687.
[54] J.P. Perdew, K. Burke, M. Ernzerhof, Generalized gradient approximation made simple, Phys. Rev. Lett. 77 (18) (1996) 3865–3868.
[55] P.E. Blöchl, Projector augmented-wave method, Phys. Rev. B. 50 (24) (1994) 17953–17979.
[56] G. Kresse, D. Joubert, From ultrasoft pseudopotentials to the projector augmented-wave method, Phys. Rev. B. 59 (3) (1999) 1758–1775.
[57] A. De Vita, The energetics of defects and impurities in metals and ionic materials from first principles, Keele University, 1992.
[58] P.E. Blöchl, O. Jepsen, O.K. Andersen, Improved tetrahedron method for Brillouin-zone integrations, Phys. Rev. B. 49 (23) (1994) 16223–16233.
[59] H.J. Monkhorst, J.D. Pack, Special points for Brillouin-zone integrations, Phys. Rev. B. 13 (12) (1976) 5188–5192.
[60] V.I. Anisimov, J. Zaanen, O.K. Andersen, Band theory and Mott insulators: Hubbard U instead of Stoner I, Phys. Rev. B. 44 (1991) 943–954.
[61] F. Zhou, C.A. Marianetti, M. Cococcioni, D. Morgan, G. Ceder, Phase separation in LixFePO4 induced by correlation effects, Phys. Rev. B - Condens. Matter Mater. Phys. 69 (2004), 201101.
[62] M.V. Ganduglia-Pirovano, A. Hofmann, J. Sauer, Oxygen vacancies in transition metal and rare earth oxides: Current state of understanding and remaining challenges, Surf. Sci. Rep. 62 (2007) 219–270.
[63] R.W. Wolfe, R.E. Newnahm, M.I. Kay, Crystal structure of Bi2WO6, Solid State Commun. 7 (24) (1969) 1797–1801.
[64] F. Wang, C. Di Valentin, G. Pacchioni, Electronic and Structural Properties of WO 3: A Systematic Hybrid DFT Study, J. Phys. Chem. C. 115 (2011) 8345–8353.
[65] S.H. Kim, S. Park, C.W. Lee, B.S. Han, S.W. Seo, J.S. Kim, I.S. Cho, K.S. Hong, Photophysical and photocatalytic water splitting performance of stibiotantalite type-structure compounds, SbMO 4 (M = Nb, Ta), Int. J. Hydrogen Energy. 37 (2012) 16895–16902.
[66] P. Sarker, M.M. Al-Jassim, M.N. Huda, Theoretical limits on the stability of single-phase kesterite-Cu2ZnSnS4, J. Appl. Phys. 117 (2015), 035702.
[67] C.M. Rost, E. Sachet, T. Borman, A. Moballegh, E.C. Dickey, D. Hou, J.L. Jones, S. Curtarolo, J.P. Maria, Entropy-stabilized oxides, Nat. Commun. 6 (2015) 8485.
[68] R.F.W. Bader, Atoms in molecules, Acc. Chem. Res. 18 (1) (1985) 9–15.
[69] G. Henkelman, A. Arnaldsson, H. Jónsson, A fast and robust algorithm for Bader decomposition of charge density, Comput. Mater. Sci. 36 (3) (2006) 354–360.
[70] E. Sanville, S.D. Kenny, R. Smith, G. Henkelman, Improved grid-based algorithm for Bader charge allocation, J. Comput. Chem. 28 (5) (2007) 899–908.
[71] W. Tang, E. Sanville, G. Henkelman, A grid-based Bader analysis algorithm without lattice bias, J. Phys. Condens. Matter. 21 (2009), 084204.
[72] M. Yu, D.R. Trinkle, Accurate and efficient algorithm for Bader charge integration, J. Chem. Phys. 134 (2011), 064111.
[73] W.H. Baur, The geometry of polyhedral distortions. Predictive relationships for the phosphate group, Acta Crystallogr. Sect. B Struct. Crystallogr. Cryst. Chem. 30 (5) (1974) 1195–1215.